Distributed Formation Control based on Bounded Voronoi Tessellation and Cable Tension for Cooperative Hovering of a Cable-Suspended Load

Saleh Abuali[1,#], Natalio Mendoza-Robles[1,2,#],
Bogdan Robu[1], Nicolas Marchand[1], Sylvain Durand[2], and Lara Briñón-Arranz[1]
[#]These authors contributed equally and are considered joint first authors.
[1]Univ. Grenoble Alpes, CNRS, Grenoble INP, GIPSA-lab, 38000 Grenoble, France [*]
[2]Univ. Strasbourg, CNRS, INSA Strasbourg, ICube, 67000 Strasbourg, France [†]

Abstract

This paper addresses the distributed formation control of N Unmanned Aerial Vehicles (UAVs) cooperatively carrying a cable-suspended payload. This is achieved using only local information, without explicit inter-agent communication, an assignment of UAVs to predefined positions in the formation, or knowledge of the load's position. The key observation is that, when hovering at the same altitude, the horizontal component of the cable tension pulls each UAV towards the position of the load's planar projection, acting as a built-in cohesion term and leaving the controller to supply only separation. We realise this separation using a bounded Voronoi tessellation-based method and derive the gain that places the team at any desired formation radius in closed form. An equilibrium analysis predicts the radius from the balance between the separation force and the cable tension. This approach has been validated through simulations and real-world flights involving four mini-UAVs.

Figure 1: Experimental setup: four Parrot MAMBO mini-UAVs cooperatively carrying a cable-suspended load. A video of the experiments is available at `youtu.be/fomDca2OPEA`.

1 Introduction

Unmanned Aerial Vehicles (UAVs) are increasingly deployed for aerial transportation, from package and medical supplies delivery to the handling of construction materials [1]. A single UAV, however, is limited by its own payload capacity; deploying several UAVs to carry a common load overcomes this limitation and yields a modular transportation system [2].

Cooperative aerial transport has been approached along a spectrum of coordination paradigms. Centralised schemes compute the team's commands from full knowledge of the system state, achieving precise load control at the cost of a single point of failure and limited scalability [3, 4]. Decentralised schemes distribute the computation across the team, typically relying on inter-agent communication to maintain a predefined geometric formation [5, 6, 7]. Fully decentralised, communication-free approaches remove this dependency, but it typically relies on tension-based control, which is sensitive to tension estimation errors [8, 9].

A recurring requirement across these methods is that the formation geometry is fixed in advance, either through a reference assigned to each agent or through prescribed inter-agent distances over a rigid graph [10]. Such a predefined assignment couples each UAV to specific partners and must be designed and certified before deployment. This motivates a complementary question: can a regular formation emerge from local interactions alone, without assigning UAVs to formation slots and without communicating absolute or relative references?

This question is naturally framed in terms of flocking. The control of a UAV swarm from local sensing is classically posed as the combination of three behaviours [11]: cohesion, separation, and alignment, of which cohesion and separation are the two that shape the formation geometry. Cohe-

[*]Email: firstname.lastname@gipsa-lab.grenoble-inp.fr
[†]Email: sdurand@unistra.fr

sion draws the agents together, while separation spreads them apart; their balance sets the spacing of the team. The key observation of this work is that, in a formation of UAVs with a cable-suspended load, cohesion need not be generated by the controller at all. The horizontal component of the cable tension pulls every UAV toward the common load point, acting as a built-in cohesion term that requires neither measurement nor communication. The controller is then left to supply only separation behavior.

For the separation behaviour, we draw on the coverage literature, where teams of agents are distributed over a region by spreading out to maximise sensing area while avoiding overlaps and blind spots. This is frequently addressed with spatial partitioning methods such as Voronoi tessellations [12], in which each agent is responsible for the region around its own position, and which operates under restricted sensing ranges to ensure decentralised, collision-free coordination [13, 14, 15]. We adopt a Bounded Voronoi Tessellation (BVT) introduced in [15] as the separation mechanism: it enforces inter-agent avoidance using only local relative positions, without online optimisation and without a predefined configuration. Combined with the tension-supplied cohesion, it yields an evenly spaced circular formation that emerges from local sensing, without communication, without predefined formation position assignments, and without knowledge of the load position.

The contributions of this paper are threefold. First, we identify and formalise, through an equilibrium analysis of the coupled UAV-load system, the horizontal cable tension as a built-in cohesion term. Second, we design a bounded-Voronoi separation law with a closed-form gain that places the formation at any desired radius, and we analyse the radial stability of the resulting equilibrium. Third, we validate the approach in simulation and in real flights with a team of Parrot MAMBO mini-UAVs.

2 PROBLEM FORMULATION

Consider a group of N identical UAVs of mass m cooperatively carrying a point-mass payload of mass m_L. UAV i is located at $\boldsymbol{p}_i \in \mathbb{R}^3$ and connected to the payload at $\boldsymbol{p}_L \in \mathbb{R}^3$ by a taut, massless cable of fixed length $l > 0$. Let $\boldsymbol{\xi}_i = \frac{\boldsymbol{p}_L - \boldsymbol{p}_i}{\|\boldsymbol{p}_L - \boldsymbol{p}_i\|}$ be the unit vector pointing from UAV i toward the payload for each $i \in \{1, \dots, N\}$. The taut cable exerts on UAV i a tension force $\boldsymbol{T}_i = \mathcal{T}_i \boldsymbol{\xi}_i$ of magnitude $\mathcal{T}_i = \|\boldsymbol{T}_i\| \geq 0$, pulling it toward the load; by reaction, the cable pulls the load toward UAV i. Each UAV carries a local sensor that estimates the relative position of neighbours within a sensing radius R (see Figure 2).

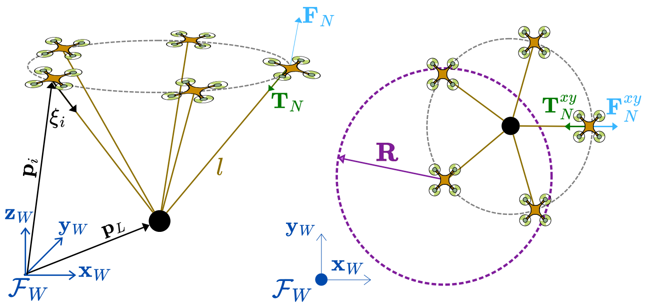

Figure 2: Overview of the cooperative load carrying system. Left: N UAVs cooperatively hover while suspending a point-mass load via taut cables of length l, where unit vectors $\boldsymbol{\xi}_i$ and tensions $\boldsymbol{T}_i$ are shown in the world frame $\mathcal{F}_W$. Right: each UAV senses the relative positions of neighbours within its sensing radius R.

2.1 System Dynamics

The simplified translational dynamics of UAV i and the payload are [9]:

$$m\,\dot{\boldsymbol{v}}_i = \boldsymbol{F}_i - mg\,\boldsymbol{z}_W + \boldsymbol{T}_i, \tag{1}$$

$$m_L\,\ddot{\boldsymbol{p}}_L = \boldsymbol{T}_{\text{res}} - m_L g\,\boldsymbol{z}_W, \qquad \boldsymbol{T}_{\text{res}} := \sum_{i=1}^{N} -\mathcal{T}_i\,\boldsymbol{\xi}_i, \tag{2}$$

where $\boldsymbol{v}_i = \dot{\boldsymbol{p}}_i$, $\boldsymbol{F}_i \in \mathbb{R}^3$ is the combined motor thrust expressed in the world frame $\mathcal{F}_W = [\boldsymbol{x}_W, \boldsymbol{y}_W, \boldsymbol{z}_W]$, where $\boldsymbol{z}_W = [0, 0, 1]^\top$ is the world vertical axis (opposing gravity), and g is gravitational acceleration. The load is driven by the resultant cable force $\boldsymbol{T}_{\text{res}}$, since each cable pulls it toward the corresponding UAV (along the direction $-\boldsymbol{\xi}_i$). We assume a low-level attitude control loop such that the thrust direction tracks its reference sufficiently fast.

2.2 Interaction Graph

The interaction of the team is described by a graph $\mathcal{G} := (\mathcal{U}, \mathcal{E})$, where $\mathcal{U} = \{1, \dots, N\}$ is the set of vertices representing the robots (UAVs) and $\mathcal{E} \subset \{(i,j) \in \mathcal{U} \times \mathcal{U} : i \neq j\}$ the set of edges (sensing links). $\mathcal{G}$ is *connected* if a path joins any two vertices. The neighbour set of robot i within a sensing radius R is defined by $\mathcal{N}_i^R := \{\, j \in \mathcal{U} : (i,j) \in \mathcal{E} \,\}$. We assume the sensing radius R is large enough that $\mathcal{G}$ remains connected throughout the mission .

2.3 Control Objective

With a view to equally distribute the load among the N UAVs, our objective is to stabilise the group of UAVs to an evenly spaced planar circular formation at a desired altitude z^{des} in a distributed manner, using only limited-range local sensing: without a predefined position assignment, and without knowledge of the load position $\boldsymbol{p}_L$. This objective concerns only the geometry of the formation and involves no global reference: the absolute positions of the group and of the load are left unconstrained, so the team may drift as a whole while the formation converges. Steering the load along a desired trajectory under the same sensing constraints is beyond the scope of this paper.

The analysis and the control design rely on the following assumptions: (A1) the cables are massless, inextensible, of identical known length l, attached to the load at a common point, and remain taut throughout the flight; (A2) all UAVs regulate the same altitude z^{des}, so the formation evolves in a horizontal plane above the load; (A3) the UAVs are identical, and m, m_L, l, N and g are known to each of them; (A4) each UAV measures the relative positions of its neighbours within the sensing radius R, together with its own position, velocity and altitude, with no inter-agent communication and no measurement of $\boldsymbol{p}_L$ or of the tensions $\boldsymbol{T}_i$; (A5) R is large enough for the sensing graph $\mathcal{G}$ to remain connected throughout the mission; (A6) a low-level attitude controller tracks the commanded thrust direction sufficiently fast, so the thrust vector $\boldsymbol{F}_i$ is treated as the control input.

3 Control Strategy

As introduced in Section 1, cohesion and separation are the two flocking behaviours that shape the formation geometry. The key observation of this work is that, in cooperative hovering with a cable-suspended load, cohesion is supplied by physics rather than by control. For a team hovering at a desired altitude z^{des}, the X–Y projection of the tension acting on UAV i is

$$\boldsymbol{T}_i^{xy} = \mathcal{T}_i \frac{\boldsymbol{p}_L^{xy} - \boldsymbol{p}_i^{xy}}{\|\boldsymbol{p}_L - \boldsymbol{p}_i\|}, \tag{3}$$

i.e., a force directed from $\boldsymbol{p}_i^{xy}$ toward the $X-Y$ load position $\boldsymbol{p}_L^{xy}$, where the $(\cdot)^{xy}$ superscript represents the X and Y components of the vector. Since all cables meet at the common load point and remain taut under the load's weight (hence $\|\boldsymbol{p}_L - \boldsymbol{p}_i\| = l$), every UAV is pulled toward a single shared point: the formation centre. Structurally, (3) is a consensus term on the horizontal positions, realised for free by the physical coupling rather than by inter-agent communication. Cohesion is thus inherent to the system, and the controller needs only supply *separation*, for which we propose the Bounded Voronoi Tessellation (BVT) method.

3.1 Separation Mechanism based on Voronoi Tessellation

In the BVT, each Voronoi region is enclosed within a 'bubble' (Figure 3). First, the method establishes the set of detected neighbours $\mathcal{N}_i^R$, within a sensing radius R centered at robot i. A Voronoi tessellation is then computed from the relative positions of the detected neighbours, partitioning the plane according to proximity. The Voronoi region of robot i is defined as follows:

$$V_i = \{\mathbf{q} \in \mathbb{R}^2 : \|\mathbf{q} - \mathbf{p}_i\| \leq \|\mathbf{q} - \mathbf{p}_j\|\,,\ \forall j \in \mathcal{N}_i^R\}, \tag{4}$$

i.e., it represents the set of points closer to $\mathbf{p}_i$ than to any other detected neighbour. We define a bubble centered on the

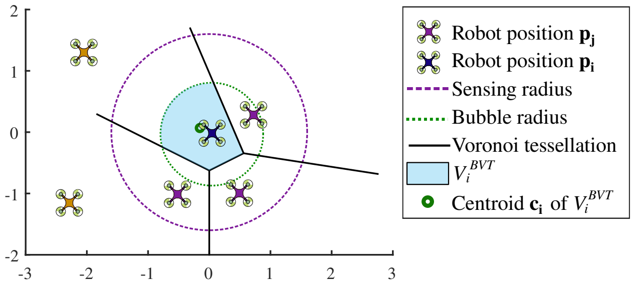

Figure 3: Bubble-based Voronoi tessellation.

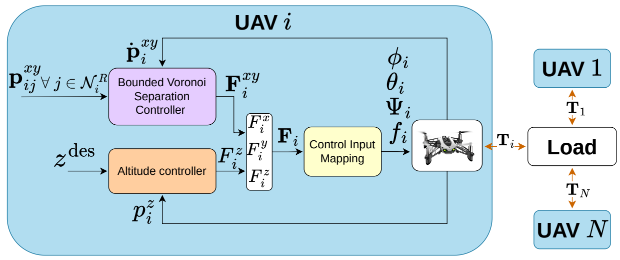

Figure 4: Control architecture. For each UAV i, the separation controller computes the horizontal force $\boldsymbol{F}_i^{xy}$ from the relative neighbour positions within the sensing radius R, and a PID altitude controller regulates the altitude via F_i^z. The resultant thrust $\boldsymbol{F}_i$ is then mapped to the UAV control inputs (tilt angles and thrust magnitude).

position of robot i, such that

$$\mathcal{B}_i = \{\mathbf{q} \in \mathbb{R}^2 : \|\mathbf{q} - \mathbf{p}_i\| \leq r_v\}, \tag{5}$$

where $r_v > 0$ is the bubble radius, which serves as the boundary for the Voronoi cell. Consequently, the safe bounded Voronoi region of each robot is the intersection of its Voronoi region with its bubble, such that

$$V_i^{BVT} = V_i \cap \mathcal{B}_i, \tag{6}$$

and the centroid of each cell V_i^{BVT} is defined as

$$\mathbf{c}_i = \frac{\int_{V_i^{BVT}} \mathbf{q}\,\rho(\mathbf{q})\,d\mathbf{q}}{\int_{V_i^{BVT}} \rho(\mathbf{q})\,d\mathbf{q}}, \tag{7}$$

where $\rho(\cdot)$ is a density function, set to a uniform $\rho \equiv 1$ in this study [16, 14].

Since the centroid represents the most isolated point within V_i^{BVT} with respect to its neighboring cells, driving UAV toward its cell centroid, $\mathbf{p}_i^{xy} \to \mathbf{c}_i$, naturally promotes separation among agents. The corresponding control law used to achieved this behavior is presented in the following section.

3.2 Control Input Design

As stated in Section 2.1, we assume direct control over the thrust vector in $\mathcal{F}_W$. The overall control architecture is shown in Figure 4. First, we regulate the altitude of each UAV with a standard PID controller acting on the altitude error, which sets the Z component of the thrust F_i^z. Then, we compute the horizontal thrust $\boldsymbol{F}_i^{xy}$ with a PD-like law that draws the UAV toward its Voronoi centroid $\boldsymbol{c}_i$, using the BVT approach as follows:

$$\boldsymbol{F}_i^{xy} = m\left(K_s(\mathbf{c}_i - \mathbf{p}_i^{xy}) - K_d\,\dot{\mathbf{p}}_i^{xy}\right), \tag{8}$$

where $\mathbf{c}_i$ is the centroid of the UAV's Voronoi cell computed in (7), and K_s, K_d are the separation and velocity-damping control gains, respectively.

Since the separation force and the horizontal tension oppose each other, the UAV does not converge to the centroid $\mathbf{c}_i$ but at an equilibrium where the two forces balance, i.e., $\|\boldsymbol{F}_i^{xy}\| = \|\boldsymbol{T}_i^{xy}\|$. We analyse this equilibrium and design K_s to achieve a desired formation radius in the following section.

4 Equilibrium Force Analysis and Formation Shaping

The equilibrium formation arises from the radial balance, in the X–Y plane, between the projection of the thrust and the projection of the cable tension (see Figure 5). Since the cables of identical length l are assumed to stay taut, every UAV is equidistant from the load, fixing a common formation radius r_c about the origin $O = \boldsymbol{p}_L^{xy}$. Assuming that the team is initialised close to a symmetric circular configuration around the load, the separation mechanism in turn spreads the UAVs evenly, yielding a uniform circular formation. The tension is fixed by the physical cable parameters, the load mass, and the number of agents; hence, for a desired formation radius $r_c^\star$, the design goal is to choose a separation gain K_s that yields $r_c = r_c^\star$.

4.1 Cable Tension in Uniform Circular Formation

At an equilibrium uniform circular formation, each UAV carries a share $m_L g/N$ of the payload weight, and the horizontal component of the cable tension is [9]

$$\|\boldsymbol{T}_i^{xy}(r_c)\| \;=\; \frac{m_L g}{N}\,\frac{r_c}{\sqrt{l^2 - r_c^2}}, \tag{9}$$

which pulls the UAV towards O and diverges as $r_c \to l$, enforcing the cable-length constraint.

4.2 Equilibrium Separation Force

For a stationary symmetric circular formation with $\dot{\mathbf{p}}_i^{xy} = \mathbf{0}$, the damping term in (8) drops out and the separation force reduces to

$$\mathbf{F}_i^{xy} = m\,K_s(\mathbf{c}_i - \mathbf{p}_i^{xy}), \tag{10}$$

directed radially outward. By symmetry, the centroid $\mathbf{c}_i$ lies on the radial axis through $\mathbf{p}_i^{xy}$; let $c_i(r_c) := \|\mathbf{c}_i - O\|$ denote its distance from the load centre O. The separation force then has magnitude $mK_s\,\sigma(r_c)$, where

$$\sigma(r_c) \;=\; c_i(r_c) - r_c \;>\; 0 \tag{11}$$

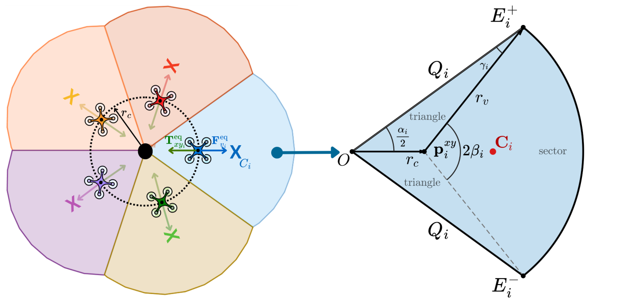

Figure 5: Decomposition of the Voronoi cells at equilibrium.

is the radial offset between UAV i and the centroid of its bounded Voronoi cell.

We evaluate $c_i(r_c)$ in the operating regime $r_v > r_c$, i.e., the bubble radius exceeds the formation radius. As described in Fig. 5, at the symmetric equilibrium, each pair of adjacent neighbours is equidistant from O, so their bisectors meet exactly at O. Each Voronoi cell is then bounded by two straight edges originating at O, with angle $\alpha_i = 2\pi/N$ and by the disk arc of radius r_v. Let $E_i^{\pm}$ be the points where the bisectors exit the disk. The equilibrium Voronoi cell $V_i^{BVT\star}$ admits an exact decomposition into *two triangles* $\triangle O\,\boldsymbol{p}_i^{xy}\,E_i^+$ and $\triangle O\,\boldsymbol{p}_i^{xy}\,E_i^-$, plus a *circular sector* $\mathcal{S}(\boldsymbol{p}_i^{xy}, r_v, 2\beta_i)$ of radius r_v centred at $\boldsymbol{p}_i^{xy}$ and spanning the angle 2β:

$$V_i^{BVT\star} \;=\; \triangle O\boldsymbol{p}_i^{xy}E_i^+ \,\cup\, \triangle O\boldsymbol{p}_i^{xy}E_i^- \,\cup\, \mathcal{S}(\boldsymbol{p}_i^{xy}, r_v, 2\beta_i). \tag{12}$$

To obtain the area of the cell, we compute the angle γ (see Figure 5) by applying the law of sines in the triangle $O\boldsymbol{p}_i^{xy}E_i^+$, with the angle $\alpha_i/2$ at O opposite the side r_v and angle γ_i opposite the side r_c. The sector half-angle β_i and the triangle side $Q_i = |OE_i^{\pm}|$ are then

$$\gamma_i = \arcsin\left(\frac{r_c\sin(\pi/N)}{r_v}\right), \tag{13}$$

$$\beta_i = \frac{\pi}{N} + \gamma_i, \tag{14}$$

$$Q_i = r_c\cos\frac{\pi}{N} + \sqrt{r_v^2 - r_c^2\sin^2\frac{\pi}{N}}. \tag{15}$$

The two triangles and the circular sector have the following area and centroid distance from O:

piece	area	centroid from O
triangle	$r_cQ_i\sin(\pi/N)$	$\dfrac{r_c + Q_i\cos(\pi/N)}{3}$
sector	$r_v^2\,\beta_i$	$r_c + \dfrac{2r_v\sin\beta_i}{3\beta_i}$

(16)

The area-weighted centroid distance from O is therefore

$$c_i(r_c) \;=\; \frac{r_cQ_i\sin\frac{\pi}{N}\cdot\frac{r_c+Q_i\cos(\pi/N)}{3} \;+\; r_v^2\beta\left(r_c + \frac{2r_v\sin\beta_i}{3\beta_i}\right)}{r_cQ_i\sin\frac{\pi}{N} + r_v^2\beta_i} \tag{17}$$

which, together with (11), fixes the equilibrium offset $\sigma(r_c)$ entering the control law.

4.3 Equilibrium Condition and Gain Design

The steady-state radial balance equates the outward separation force to the inward tension at $\dot{\mathbf{v}}_i = \mathbf{0}$:

$$\|\boldsymbol{F}_i^{xy}\| = \|\boldsymbol{T}_i^{xy}(r_c)\|$$
$$m\,K_s\,\sigma(r_c) \;=\; \frac{m_L g}{N}\,\frac{r_c}{\sqrt{l^2 - r_c^2}}. \tag{18}$$

To achieve a desired circular formation of radius $r_c^\star$, we solve (18) for the separation gain,

$$K_s \;=\; \frac{m_L g}{mN}\,\frac{r_c^\star}{\sqrt{l^2-(r_c^\star)^2}}\,\frac{1}{\sigma(r_c^\star)}. \tag{19}$$

The balance (18) admits a single equilibrium radius. As r_c grows, the tension term (9) increases monotonically and diverges at $r_c = l$, while the separation offset $\sigma(r_c)$ decreases as the cell spreads wider, and its centroid is drawn inward. The two curves therefore cross exactly once, and the crossing is stable: an outward perturbation raises the tension and lowers the separation, restoring the UAV inward, and vice versa, so the formation self-regulates to a single radius without explicit radius feedback.

4.4 Stability of the Equilibrium Formation

The equilibrium has two independent modes: the formation *radius* and the *angular* spacing of the UAVs. This work focuses on the radial mode, which the gain design (19) directly shapes; the angular spacing is a consequence of the separation mechanism, as discussed below.

At fixed angular positions, each UAV moves radially under the balance between the outward separation force $mK_s\,\sigma(r_c)$ and the inward horizontal tension $\|\boldsymbol{T}_i^{xy}(r_c)\|$. As r_c increases, the tension (9) grows steadily and diverges at $r_c = l$, while the separation offset $\sigma(r_c)$ decreases as the Voronoi cell spreads wider and its centroid is drawn inward. The two terms therefore intersect at a single radius, the designed $r_c^\star$ of (19), and this intersection is stable: an outward perturbation raises the tension and lowers the separation, pulling the UAV back inward, while an inward perturbation does the reverse. The velocity damping term $-mK_d\dot{\boldsymbol{p}}_i^{xy}$ in (8) damps the resulting radial motion, so the formation self-regulates to $r_c^\star$ without explicit radius feedback.

The angular spacing is handled by the same separation mechanism: when $\alpha_i \neq 2\pi/N$, the Voronoi cell centroid $\mathbf{c}_i$ has a tangential component that drives the UAV toward the wider gap, so equal angular spacing $\alpha_i = 2\pi/N$ is the configuration in which this component vanishes. The formation orientation about $\boldsymbol{z}_W$ remains free, as no UAV measures an absolute angle. Accordingly, the experimental analysis that follows evaluates the radial behaviour through the formation radius $\hat{r}_c$, and does not separately characterise the angular spacing.

5 SIMULATION AND EXPERIMENTAL RESULTS

This section presents both the simulation and the experimental results of our Bounded Voronoi-based formation control approach.

As mentioned in Section 4, to start the controller near equilibrium and avoid a local minimum where one UAV ends up at the centre of the formation [15] (which slackens its cable), the UAVs first take off and hover on a predefined circular formation of radius 0.6 m above the load using a standard PID position controller. The position controller is then switched off and replaced by the proposed Voronoi-based separation controller (8), whose gain K_s is computed from (19) for the desired radius $r_c^\star$. No position reference is given after the switch: the formation expands or contracts purely under the balance between the separation force and the cable tension, and it is stabilised at the desired equilibrium radius.

5.1 Control Input Mapping

The designed control input throughout the paper has been the thrust vector $\boldsymbol{F}_i$. For our mini-UAVs, however, the actual control inputs to each UAV are the tilt angles (roll ϕ_i, pitch θ_i, and yaw ψ_i) together with the thrust magnitude f_i. Since yaw can be managed separately, we assume without loss of generality that $\psi_i = 0$ for all UAVs. The control input $\mathbf{U}_i = [\phi_i, \theta_i, \psi_i, f_i]^\top$ is then retrieved by decomposing $\boldsymbol{F}_i$ into a thrust magnitude and tilt angles. Adopting the Z–Y–X Euler convention, in which UAV i executes the rotations ψ_i, θ_i, ϕ_i in turn, gives

$$\phi_i = \operatorname{atan2}\!\left(F_i^y,\, \sqrt{{F_i^z}^2 + {F_i^x}^2}\right) \tag{20}$$
$$\theta_i = \operatorname{atan2}(F_i^x,\, F_i^z) \tag{21}$$
$$f_i = \|\boldsymbol{F}_i\|, \tag{22}$$

where $\operatorname{atan2}$ is the two-argument arc-tangent function.

5.2 Formation Radius Estimation

In real experiments, the UAVs may converge to uneven angular spacing around the circle; we therefore estimate the formation radius as the mean radial distance to the load centre, which is insensitive to how the UAVs are distributed around it. As established in Section 4, the relevant radius is the offset from the load centre $O = \mathbf{p}_L^{xy}$, so we use the load position provided by the motion-capture system (only for evaluation, not in the control loop) and compute the individual radii $r_i(t)$ for each UAV

$$r_i(t) = \|\mathbf{p}_i^{xy}(t) - \mathbf{p}_L^{xy}(t)\|, \tag{23}$$

and the estimated circular formation radius

$$\hat{r}_c(t) = \frac{1}{N}\sum_{i=1}^{N}\left\|\mathbf{p}_i^{xy}(t) - \mathbf{p}_L^{xy}(t)\right\|. \tag{24}$$

The steady-state accuracy is then quantified by the root-mean-square (RMS) error between the estimated and the desired radius,

$$e_{\mathrm{RMS}} = \sqrt{\frac{1}{M} \sum_{t_k \in [t_1,\, t_2]} \left(\hat{r}_c(t_k) - r_c^{\star} \right)^2}, \tag{25}$$

where $[t_1,\, t_2]$ is a steady-state window and M is the number of motion-capture samples it contains.

5.3 *Simulation results*

To test the proposed control approach in simulation, we use a Matlab/Simulink simulator that includes a realistic model of the Parrot MAMBO mini-UAVs, with the full nonlinear dynamics and the experimentally identified closed-loop angle and thrust dynamics from [9]. The cables are modelled as rigid, massless bars that transmit force between each UAV and the load.

To validate the closed-form gain design (19), we simulate the system for several desired radii $r_c^{\star} \in \{0.5, 0.6, 0.7, 0.8, 0.9, 1.0\}$ m; from (19), the corresponding separation gain for each case is recomputed as $K_s \in \{0.4835, 0.6261, 0.7961, 1.0037, 1.2639, 1.6018\}$. The simulated team consists of $N = 5$ UAVs of mass $m = 78.5$ g cooperatively carrying a point-mass load of $m_L = 50$ g through identical cables of length $l = 1.5$ m. The bubble radius is set to $r_v = 1.8$ m and the sensing radius to $R = 2.8$ m.

Figure 6 shows the time evolution of the estimated formation radius $\hat{r}_c$ (24) for each desired radius. During the first phase (t = 0–10 s) the PID position controller holds the team on the 0.6 m hovering circle; at the switch the formation expands or contracts purely under the imbalance between the separation force and the cable tension, and settles at the designed radius. The realised steady-state radius exactly matches the design value across all tests, confirming that the equilibrium analysis of Section 4 correctly predicts the closed-loop geometry.

5.4 *Real-World Experiments*

For the real-world experiments, we use a set of Parrot MAMBO mini-UAVs in a flight arena equipped with a motion-capture (MoCap) system. The decentralised control strategy is emulated within a centralised Matlab/Simulink framework. While the MoCap system provides global position measurements for all UAVs, local sensing is reproduced by constructing an individual neighbor set for each agent. Specifically, for UAV i, only agents whose distance to UAV i is less than or equal to the sensing radius R are included in its neighborhood and used in the control-law evaluation. Each UAV also has access to its own position and velocity estimates. The computed control inputs are then transmitted to each UAV over a Bluetooth link.

The experimental platform consists of $N = 4$ Parrot MAMBO mini-UAVs attached to a common point-mass load of $m_L = 33.5$ g by cables of identical length $l = 1.4$ m (see Figure 1). The sensing radius is set to $R = 3$ m, the bubble

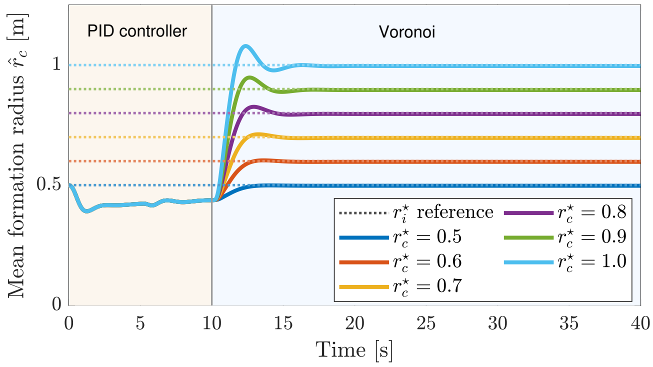

Figure 6: Simulation with $N = 5$ UAVs: estimated formation radius $\hat{r}_c$ (24) for six desired radii $r_c^{\star} \in \{0.5, \ldots, 1.0\}$ m (solid), with the corresponding references (dotted). The shaded regions mark the PID hovering phase and the proposed Voronoi-based controller.

radius to $r_v = 1.5$ m, and the separation gain $K_s = 1.0423$ computed from (19) for the desired radius $r_c^{\star} = 0.7$ m.

The experiment is divided into three phases, marked by the shaded regions in Figure 7. First (0–7 s), the four UAVs take off freely from the ground. Second (7–15 s), they lift the load and hover on a circle of radius 0.6 m at the desired altitude using a PID position controller; the cables become taut and the load is airborne by the end of this phase. Once the load is airborne, the horizontal tension component (3) acts on each UAV as an inward disturbance that the position controller does not compensate perfectly, so the realised hovering radius settles below the commanded 0.6 m circle (visible in Figure 7 before $t = 15$ s); the same effect appears in the simulation of Figure 6. This residual offset is a manifestation of the tension-supplied cohesion exploited by the proposed approach. Third (from $t = 15$ s), the position controller is switched off and replaced by the Voronoi-based separation controller (8), and the formation is left to self-regulate with no position reference and no knowledge of the load position. Since the designed equilibrium radius exceeds the hovering one, the switch produces a visible expansion of the formation, driven only by the imbalance between the centroid offset and the cable tension.

5.5 *Analysis of the Results*

Figure 7 shows the time evolution of the estimated radius $\hat{r}_c$ from (24) together with the individual radii r_i from (23). After the switch at $t = 15$ s, the formation expands from the hovering configuration and converges to the designed radius with no position reference, settling at a mean of $\hat{r}_c = 0.690$ m over the window t = 22–32 s, with an RMS error of 2.0 cm with respect to $r_c^{\star} = 0.7$ m, i.e. 2.8% of the desired radius, reached purely through the balance between the cable tension and the Voronoi-based separation. The mean radius therefore matches the design value closely, while the individual

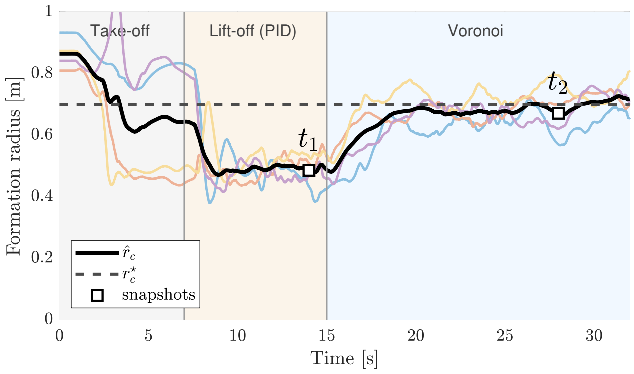

Figure 7: Experiment with 4 Parrot MAMBO mini-UAVs for $r_c^\star = 0.7$ m: estimated formation radius $\hat{r}_c$ (24) (solid black), individual radii r_i (thin), and desired radius (dashed). The shaded regions mark the three phases: free take-off, lift-off with the load under the PID position controller, and the proposed Voronoi-based controller. The square markers indicate the snapshot instants t_1 and t_2 of Figure 8.

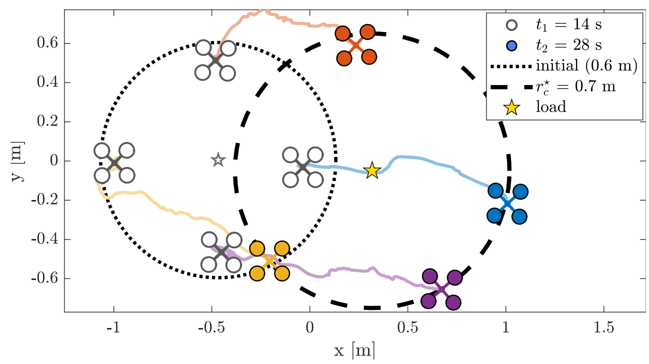

Figure 8: Top view of the experiment with 4 Parrot MAMBO UAVs at two instants: $t_1 = 14$ s, the predefined 0.6 m hovering circle under the PID controller (just before the switch), and $t_2 = 28$ s, the expanded formation under the Voronoi-based controller, near the designed radius $r_c^\star = 0.7$ m. The star marks the load centre O.

radii differ from one another: under taut cables at a common altitude, $r_i = \sqrt{l^2 - h_i^2}$ with h_i the height of UAV i above the load, so the imperfect altitude tracking of each UAV causes a radial offset. The spread of the individual radii r_i around $\hat{r}_c$ also reflects the angle biases of the UAVs, whose realised tilt angles differ from the commanded ones, $\theta^{\text{real}} = \theta^{\text{command}} + \theta^{\text{bias}}$, together with hardware differences such as battery health and propeller wear.

Figure 8 gives the corresponding top view through two formation snapshots. At $t_1 = 14$ s, just before the switch, the UAVs maintain the predefined 0.6 m circle under the PID position controller; at $t_2 = 28$ s, after convergence of the Voronoi-based controller, the formation has expanded to the designed radius $r_c^\star = 0.7$ m, driven only by the tension–separation balance. The UAVs do not form a perfectly uniform circle due to the differing biases of each UAV.

6 CONCLUSIONS

This paper presents a distributed strategy for cooperative hovering cable-suspended payload by N UAVs, in which the team self-organises into an evenly spaced circular formation using only local sensing. The key finding is that the horizontal component of the cable tension acts as a built-in cohesion term, meaning that the controller only needs to supply separation. This was achieved using a bounded Voronoi-based controller with a closed-form gain that positions the formation at any desired radius.

This approach was validated through simulations and real-world flights involving four Parrot MAMBO mini-UAVs. In these experiments, the team converged to the designed radius with an RMS error of 2.8%, without any position reference, predefined assignment or knowledge of the load position. The main limitations are twofold. First, the controller contains no global objective, so the absolute position of the group is unconstrained and the team drifts as a whole. Second, the gain design in (19) requires knowledge of the load mass m_L and the number of agents N. Building upon the payload-carrying framework presented in this work, future research will focus on analysing the stability of the formation during motion and extending the approach to the payload transportation problem. Furthermore, distributed estimation techniques will be developed to infer the load mass and the number of agents online using only local measurements.

ACKNOWLEDGEMENTS

This work has been partially supported by the French National Research Agency in the context of the muteSWARM project (ANR-23-IAS2-0004) and the French National Research Infrastructure ROBOTEX 2.0 (Grants ROBOTEX ANR-10-EQPX-44-01 and TIRREX ANR-21-ESRE-0015).

REFERENCES

[1] Ladfah Gantiya and Chuchart Pintaviooj. Medical delivery drone. In *2024 16th Biomedical Engineering International Conference (BMEiCON)*, pages 1–6, 2024.

[2] Taeyoung Lee. Geometric control of quadrotor UAVs transporting a cable-suspended rigid body. *IEEE Transactions on Control Systems Technology*, 26(1):255–264, 2018.

[3] Taeyoung Lee, Koushil Sreenath, and Vijay Kumar. Geometric control of cooperating multiple quadrotor UAVs with a suspended payload. In *52nd IEEE Conference on Decision and Control*, pages 5510–5515, 2013.

[4] Sihao Sun, Xuerui Wang, Dario Sanalitro, Antonio Franchi, Marco Tognon, and Javier Alonso-Mora. Agile and cooperative aerial manipulation of a cable-suspended load. *Science Robotics*, 10(107), 2025.

[5] Xiaozhen Zhang, Fan Zhang, Panfeng Huang, Jiale Gao, Hang Yu, Chongxu Pei, and Yizhai Zhang. Self-triggered based coordinate control with low communication for tethered multi-UAV collaborative transportation. *IEEE Robotics and Automation Letters*, 6(2):1559–1566, 2021.

[6] Nicola De Carli, Riccardo Belletti, Emanuele Buzzurro, Andrea Testa, Giuseppe Notarstefano, and Marco Tognon. Distributed nmpc for cooperative aerial manipulation of cable-suspended loads. *IEEE Robotics and Automation Letters*, 10(10):10546–10553, 2025.

[7] Natalio Mendoza-Robles, Alfredo Namigtle-Jiménez, Pierre Susbielle, Nicolas Marchand, Sylvain Durand, Rogerio Enríquez-Caldera, Lara Briñón-Arranz, and José Fermi Guerrero-Castellanos. Cooperative control of multirotor UAVs with disturbance rejection capabilities for load transportation. *IEEE Access*, 14:67204–67217, 2026.

[8] C. Gabellieri, M. Tognon, D. Sanalitro, and A. Franchi. Force-based pose regulation of a cable-suspended load using UAVs with force bias. In *2023 IEEE/RSJ International Conference on Intelligent Robots and Systems (IROS)*, pages 6920–6926, 2023.

[9] Saleh Abuali, Kostas Skantzikas, Pierre Susbielle, Nicolas Marchand, and Lara Briñón-Arranz. Communication-free cooperative transportation with multiple UAVs. *IFAC-PapersOnLine*, 59(18):187–192, 2025.

[10] Héctor García de Marina and Ewoud Smeur. Flexible collaborative transportation by a team of rotorcraft. In *2019 International Conference on Robotics and Automation (ICRA)*, pages 1074–1080, 2019.

[11] Reza Olfati-Saber. Flocking for multi-agent dynamic systems: Algorithms and theory. *IEEE Transactions on Automatic Control*, 51(3):401–420, 2006.

[12] J. Cortés, S. Martínez, T. Karatas, and F. Bullo. Coverage control for mobile sensing networks. *IEEE Transactions on Robotics and Automation*, 20(2):243–255, 2004.

[13] Meng Zhou, Jianyu Li, Chang Wang, Jing Wang, and Li Wang. Applications of Voronoi Diagrams in Multi-Robot Coverage: A Review. *Journal of Marine Science and Engineering*, 12(6):1–21, 2024.

[14] Federico Pratissoli, Beatrice Capelli, and Lorenzo Sabattini. On Coverage Control for Limited Range Multi-Robot Systems. In *2022 IEEE/RSJ International Conference on Intelligent Robots and Systems (IROS)*, pages 9957–9963. IEEE, 2022.

[15] Natalio Mendoza-Robles, Lara Briñón-Arranz, Pierre Susbielle, Kostas Skantzikas, Sylvain Durand, and Nicolas Marchand. Distributed formation control with local sensing combining Bubble-based Voronoi tessellation and consensus. In *2026 International Conference on Unmanned Aircraft Systems (ICUAS)*, pages 805–812, 2026.

[16] Vladimir Alexandrov, Konstantin Kirik, and Alexander Kobrin. Multi-robot Voronoi tessellation based area partitioning algorithm study. *Paladyn, Journal of Behavioral Robotics*, 9:214–220, 2018.